Effects of fluorination on the structure, magnetic and electrochemical properties of the P2-type Na_xCoO_2 powder

Dragana Jugović[1*], Miloš Milović[1], Maja Popović[2], Vladan Kusigerski[2], Srečo Škapin[3], Zlatko Rakočević[2], and Miodrag Mitrić[2]

[1]Institute of Technical Sciences of SASA, Knez Mihailova 35/IV, 11 000 Belgrade, Serbia

[2]Vinča Institute of Nuclear Sciences, University of Belgrade, P.O. Box 522, 11 001 Belgrade, Serbia

[3]Jožef Štefan Institute, Jamova 39, SI-1000 Ljubljana, Slovenia

*Corresponding author: Dragana Jugović

Phone: +381641177549,

e-mail: dragana.jugovic@itn.sanu.ac.rs; djugovic@vinca.rs

Abstract

The main goal of this research has been to investigate for the first time the effects of fluorination on the crystal structure, magnetic, and electrochemical properties of the P2-type Na_xCoO_2 powder. Sodium cobalt oxide with a P2-type structure is synthesized by a modified solid-state reaction consisting of alternating processes of rapid heating up to 750 ºC and rapid cooling to the room temperature. The obtained powder is fluorinated using a gas-solid reaction with NH_4HF_2 as

fluorinating agent. Fluorination causes a decrease of sodium content in the parent phase with the concurrent formation of the minor phases of Na_2CO_3 and NaF. The structure of Na_xCoO_2 in both powders is refined in $P6_3/mmc$ space group. The results of the Rietveld refinement combined with the findings from the XPS measurements confirm the $Na_{0.76}CoO_2$ and $Na_{0.44}CoO_{1.96}F_{0.04}$ stoichiometries for the pristine and fluorinated powders, respectively, which indicates that 4 at.% of fluorine ions per formula unit are incorporated in the structure. Preliminary electrochemical investigations have revealed an improved charge/discharge performance. The influence of fluorination on morphology and magnetic properties has also been examined.

Keywords: Energy storage materials; Gas–solid reactions; Crystal structure; X-ray diffraction; Photoelectron spectroscopies; Magnetic measurements

1. Introduction

The rising demands for energy storage systems increase the interest in sodium-ion batteries as an alternative to lithium-ion batteries [1]. Layered sodium transition metal oxides ($Na_xT_MO_2$, T_M has one or more transition metal cations) have been extensively studied as cathode materials for sodium-ion batteries [2]. Na_xCoO_2 is the most attractive among them due to its characteristics: an unusually large thermopower [3, 4], interesting magnetic properties [5], and its hydrated compound shows superconductivity below 5 K [6].

Na_xCoO_2 can crystallize in several layered structures depending on sodium content, oxygen partial pressure and temperature [7]. In each of them, the edge-sharing CoO_6 octahedra form $(CoO_2)_n$ sheets, between which sodium ions are inserted with octahedral or prismatic

surroundings [8]. The packing also differs in the number of sheets (2 or 3 sheets) within the unit cell, i.e. AB CA BC, AB BA, and AB BC CA oxygen packing, revealing three possible structural types: O3, P2, and P3, respectively [9]. The P2 type of structure is considered to be the most suitable structure for the electrochemical application, as an energy storage material. Within the P2 structure, the Na^+ ions are intercalated in a trigonal prismatic environment between adjacent $(CoO_2)_n$ sheets, taking one of two possible positions denoted as Na(1) and Na(2) (Figure 1). Cobalt ions lie above and below Na(1) sites. Na(1) shares faces only with two CoO_6 octahedra of the adjacent sheets, whereas Na(2) shares edges with the six surrounding CoO_6 octahedra [10]. Since the distance between the adjacent Na(1) and Na(2) sites is two times smaller than the ionic radius of Na, simultaneous occupancy of the nearest-neighboring sites is not possible. From an electrostatic point of view, a Na(1) site is expected to be less stable than a Na(2) site. Stoichiometric reasons do not require the presence of sodium ions at a Na(1) site; however, the simultaneous occupation of both sites leads to stable configurations through the minimization of the in-plane Na^+–Na^+ electrostatic repulsion [11]. The magnetic properties of Na_xCoO_2 phases strongly depend on the sodium content (x). The composition with x~ 2/3 follows the Curie-Weiss law; with the further decrease in x, Na_xCoO_2, changes from a "Curie-Weiss metal" to a "paramagnetic metal" through an insulating charge-ordered state about x=0.5 [12]. An unusual low-temperature (22 K) magnetic phase transition is observed in the composition with x = 0.75 [13].

The galvanostatic electrochemical curve of the P2 type Na_xCoO_2 has a complex profile: it consists of several voltage plateaus, which imply the existence of biphasic domains, potential drops that are related to stable single-phase domains, and the sloping parts that are typical of solid-solution behaviour [10,14]. This is a consequence of the Na-vacancy ordering and the

resulting structural response of the CoO_2 layers to changes in the electron count and Na ion distribution [15].

Numerous studies on cation doping seek to improve the performance of sodium transition metal oxides with a P2-type structure [16–21]. Fluorine doping has been demonstrated to enhance electrochemical properties of various cathode materials for lithium-ion batteries [22–27]. On the other hand, to the best of our knowledge, there are no reports on anion doping of the P2-type Na_xCoO_2. The main goal of this research has been to investigate for the first time the possibility of fluorine doping of the P2-type Na_xCoO_2 powder and to examine the effects that fluorination has on its crystal structure, magnetic, and electrochemical properties.

2. Experimental

2.1. Synthesis of a pristine Na_xCoO_2

A solid state reaction was used for the preparation of the pristine Na_xCoO_2 powder. Na_2CO_3 and Co_3O_4 were mixed in the molar ratio 1.7 : 1 (the targeted stoichiometry was 0.75 sodium per cobalt, but due to sodium volatility, Na_2CO_3 was added in excess) and thoroughly grounded in a mortar. The precursor powder was not pelletized; it was placed in the powder form in a platinum crucible and then subject to a high-temperature treatment. As opposed to the conventional solid-state method, which involves long-term heating, our research relied on the method of sequential cycles of rapid heating and cooling, with an intermediate grinding stage between two cycles. In one cycle, the precursor powder was rapidly heated to 750 ºC in air with a dwell time of 15

minutes and then air-quenched to room temperature. This was done to reduce both the preferential orientation during the particle growth and sodium volatilization. Fourier transform infrared (FTIR) spectra and XRD patterns were collected after each cycle to monitor both the stage of the solid-state reaction and the potential presence of impurities. Namely, after the initial grinding of the reactants, the long-range order in Na_2CO_3 broke and it became undetectable by XRD. However, a short-range order was preserved, due to which Na_2CO_3 could easily be detected by FTIR spectroscopy. The final powder that was subsequently fluorinated, denoted as NCO, was obtained after 12 cycles, which corresponded to 3 hours of the high-temperature treatment. The guiding criterion was to obtain the powder containing no or a minimal amount of impurity phases (Co_3O_4 and Na_2CO_3). Interestingly, an XRD analysis of the powder obtained after seven 15-minute intervals of thermal treatment showed phase purity, but FTIR revealed the remains of the Na_2CO_3 phase. Due to this, the alternating processes of heating and cooling had been prolonged until FTIR confirmed the absence of the Na_2CO_3 phase. The evolution of FTIR spectra during synthesis is presented in Supporting Information, Figure S1.

2.2. Synthesis of F-doped Na_xCoO_2

Several approaches were used in the synthesis of F-doped Na_xCoO_2. The first unsuccessful attempt was a solid-state reaction of stoichiometric amounts of Na_2CO_3, Co_3O_4, and NaF at 900 ºC for 20 hours in air. Beside the Na_xCoO_2 phase, NaF and Co_3O_4 were still present. By rising the temperature to 950 ºC, Na_xCoO_2 started to decompose and at 1000 ºC both Na_xCoO_2 and NaF phases vanished, while CoO emerged (Supporting Information, Figure S2). Similar results were

obtained by varying the precursors. A solid-state reaction between NH_4CoF_3 and Na_2CO_3 at 800 ºC in air resulted in the formation of NaF, Co_3O_4 and CoO phases.

Another approach was also tested: the fluorination of the previously synthesized Na_xCoO_2 with NH_4HF_2 as a fluorination agent – a method standardly used for the fluorination of Sr_2CuO_3 [28] and rare-earth oxides [29,30]. Na_xCoO_2 and NH_4HF_2 were thoroughly mixed and then introduced to different temperatures (from 450 - 800 ºC), but NaF was always allocated as a separate phase. However, when the fluorination was conducted at 200 °C, in a vacuum evacuated atmosphere, a routine XRD check revealed the absence of the NaF phase, as well as a significant shift of diffraction peaks. Therefore, this method was adopted for the fluorination process. The requred amounts of Na_xCoO_2 and NH_4HF_2 were placed in two separated teflon-lined containers, so as to avoid contact of the reagents either in the solid or in the liquid form, and to enable only the vapor-solid reaction. After vacuuming the system, the temperature was raised to 200 °C with a dwell time of two hours, and before spontaneous cooling, it was vacuumed again to prevent the contamination of the powder with the remains of NH_4HF_2 and NH_4F vapors. The obtained powder will hereinafter be referred to as the NCOF sample.

2.3. Materials characterization

X-ray powder diffraction measurements were used for both the phase purity check and the structural analysis of the synthesized samples. The diffraction data were collected on a Philips PW 1050 diffractometer with Cu-K$\alpha_{1,2}$ radiation (Ni filter) at room temperature. The measurements were done in a 2θ range of 10–70° with a scanning step width of 0.05° and 3 s time per step, for routine phase checking; for the crystal structure refinement, the 2θ range was

10–110° with a scanning step width of 0.02° and 14 s time per step. The crystal structure refinement was based on the Rietveld full profile method [31] using the Koalariet computing program, based on the fundamental parameters convolution approach in diffraction-line-profile fitting [32].

The FTIR spectra of the samples were recorded in ambient conditions in the mid-IR region (400–4000 cm^{-1}) with a Nicolet IS 50 FT-IR Spectrometer operating in the ATR mode and the measuring resolution of 4 cm^{-1} with 32 scans.

The morphologiy of the synthesized powders was analyzed by Field-Emission Scanning Electron microscopy (FE-SEM, Supra 35 VP, Carl Zeiss).

The XPS analysis was carried out on a SPECS customized UHV surface analysis system containing a sputter ion gun, PHOIBOS 100 spectrometer for energy analysis, dual anode Al/Ag monochromatic source and electron flood gun. The XPS survey spectra were taken using a monochromatic Al Kα line (photon energy of 1486.74 eV) in the FAT 40 mode with an energy step of 0.5 eV and a dwell time of 0.2 s. High-resolution spectra were recorded in the FAT 20 mode with an energy step of 0.1 eV and a dwell time of 2 s.

The magnetization measurements were performed using a superconducting quantum interference device (SQUID) magnetometer (Quantum Design MPMS XL XL-5) in the 4–300 K temperature range in an applied field of 100 Oe.

The electrochemical measurements were carried out in a closed, argon-filled two-electrode cell at room temperature, with metallic sodium as a counter electrode. A 1M-solution of $NaClO_4$ in propylene carbonate (PC, Aldrich) was used as an electrolyte. $NaClO_4$ was obtained by the vacuum drying of $NaClO_4 \cdot H_2O$ (p.a., J. T. Baker) at 170 ºC. The working electrodes were prepared by mixing the synthesized material, carbon black and polyvinylidene fluoride (PVdF,

Aldrich) in the weight ratio 75:15:10, respectively, with N-methyl-2-pyrrolidone to form a slurry that was afterward deposited on platinum foils. Galvanostatic charge/discharge tests were performed within the potential range of 2 – 3.8 V at C/10 current rates by using Vertex.One (Ivium Technologies) potentiostat.

3. Results and Discussion

3.1. Morphology study

The morphologies of the synthesized powders, determined by FESEM, were basically similar, consisted of strongly agglomerated polyhedral particles (Figures 2a and 3a). The particles of the fluorinated powder were smaller in size than the particles of the pristine powder. In some zones of both samples, larger particles with a laminar structure could be observed, as well (Figures 2b and 3b). Also, in the fluorinated powder rod-like particles could be observed (Figure 3) which probably originated from the Na_2CO_3 impurity phase revealed by FTIR.

3.2. XRD analysis

Routine X-ray powder diffraction measurements for phase identification confirmed only the presence of a P2-type Na_xCoO_2 phase in both powders. However, there were notable differences in X-ray diffractograms: the shift of the diffraction maxima, the change of the relative peak intensity ratio, and the peak broadening observed for the fluorinated sample. These could be ascribed to the sodium deficiency and/or to the incorporation of fluorine ions. The fluorinated powder also contained the Na_2CO_3 impurity phase, revealed only by the FTIR analysis.

The structures of both the pristine and the fluorinated Na_xCoO_2 powders were refined according to the high-symmetry model (space group $P6_3/mmc$ no. 194). In the $P6_3$/mmc hexagonal space

group, Na atoms were placed in the centers of prisms at the 2*b* [[0, 0, 1/4]] Wyckoff positions with site symmetry $\bar{6}m2$ and the 2*d* [[1/3, 2/3, 3/4]] Wyckoff positions with site symmetry $\bar{6}m2$ (D_{3h}), denoted as Na(1) and Na(2) sites, respectively; Co ions were fixed at the octahedral 2*a* [[0, 0, 0]] Wyckoff positions with site symmetry$\bar{3}m$ (D_{3d}), while oxygen O^{2-} ions were positioned at the 4*f* [[1/3, 2/3, z]] Wyckoff positions with site symmetry 3*m* (C_{3v}). Fluorine ions were free to occupy the oxygen site. Due to a strong correlation, isothermal temperature factors were kept fixed during the refinement. Their values were adopted from the neutron powder diffraction refinement of Na_xCoO_2 [15]. The value of the *z* coordinate at the O(F) position was refined as far as all other ions are in special positions. A longer diffraction data acquisition period revealed an additional NaF phase in the fluorinated powder accordingly,the two phases were included in the refinement of the NCOF sample. For both samples the Na content in the Na_xCoO_2 phase was unambiguously determined through structural refinement.

The results of the Rietveld refinement are given in Figure 4 and Tables 1 and 2. The obtained lattice parameters for pristine Na_xCoO_2 were in good agreement with the literature data [33]. Fluorination caused a small decrease of the lattice parameter *a* and an increase of the lattice parameter *c* (Table 1). This trend of changes in lattice parameters is common during sodium deintercalation [10, 15] as decreased sodium concentration increases the spacing between adjacent oxygen layers. In addition, the NCOF powder had smaller crystallites, with an increased NaO_2 interslab distance and a decreased CoO_2 slab thickness (Table 1). O–Co–O angles and Co–O distance define CoO_2 slab thickness which determines electron structure. The change of O–Co–O angles and a decrease of Co-O distance (Table 2) correspond to the compression of the CoO_2 layers along the c-axis which usually gives wider bands, smaller effective mass and enhanced electron conductivity [15].

The refinement of the occupancies of both sodium sites revealed that the Na/Co ratio was of 0.76 and 0.44 for the pristine and fluorinated powders, respectively. Apparently, during fluorination, a part of sodium ions migrated from the lattice and formed both a distinct NaF phase (in the amount of 2.8 wt.%) and a Na_2CO_3 phase (revealed only by FTIR). The obtained lattice parameters for the NCOF sample deviated from the literature data for sodium concentrations around 0.44 [15, 34]. In addition, the interslab distance, taken as a measure of the sodium content, also implied a higher sodium content [35]. As the Na(1) site shared faces with the octahedron around Co cations, the Na(1) site had a larger site energy than the Na(2) site due to the direct repulsion between Na and the adjacent Co ions [33]. The smaller site energy of the Na(2) site causes the preferred occupancy of the Na(2) site over the Na(1) site, as observed in this investigation. This difference in site energies was expressed in the Na(1)/Na(2) ratio and it was a strong function of total Na content. The Na(1)/Na(2) ratio for the NCO sample (0.48) was in accord with the literature data for the given sodium concentration [15], while its value for the NCOF sample (0.63) corresponded to a sodium content higher than the refined value [36], which was equivalent to a smaller average oxidation state of cobalt. Apart from the extraction of sodium ions from the lattice, this further implies that fluorination additionally modified the average oxidation state of cobalt through tiny fluorine incorporation in the lattice, as revealed by structural refinement (Table 1).

3.3. XPS analysis

More information on the cobalt oxidation state was provided by XPS experiments. The survey photoelectron spectra of both powders show the presence of the Co 2*p*, O 1*s*, and Na 1*s* peaks, as well as the presence of an F 1*s* peak in the fluorinated powder (Figure 5). High-resolution scans of constituent elements (Co, O, and Na) are compared in Figure 6. The Co 2*p* spectra of both

powders consist of two major lines, Co $2p_{3/2}$ and Co $2p_{1/2}$ from spin-orbital splitting, and the satellite shake-up lines (Table 3). The main doublet of the pristine powder (779.8 – 794.9 eV) is assigned to Co^{3+} ions and it is well-documented in the literature [37,38]. The binding energy of the second doublet (781.1 – 796.4 eV) is ascribed to Co^{4+} ions, which is less commonly presented in the literature [39,40]. The presence of Co^{2+} can be excluded [41]. The deconvoluted XPS spectrum of the fluorinated powder contains components with almost the same binding energies as the pristine powder (Table 3), but with different intensity ratios. The peak area ratio of the two doublets has the Co^{3+}: Co^{4+} ratio equal to 0.76 : 0.24 and 0.48 : 0.52 for the pristine and the fluorinated powder, respectively. The average oxidation numbers of cobalt ions, calculated from the above Co^{3+}:Co^{4+} proportions, are +3.24 and +3.52 for the pristine and the fluorinated powders, respectively. The oxidation number of cobalt in the fluorinated powder is smaller than the expected value for the given Na/Co ratio. This is a solid proof that some fluorine ions are incorporated in the lattice. Taking in account both the sodium occupancies, determined by the structural refinements, and the average oxidation state of cobalt, calculated from the XPS measurements, the derived compositions of the pristine and the fluorinated powders are $Na_{0.76}CoO_2$ and $Na_{0.44}CoO_{1.96}F_{0.04}$, respectively. The calculated fluorine content is in agreement with the refined fluorine occupancy of the oxygen site (Table 1): taking into account the multiplicity of the oxygen site, the fluorine content per formula unit obtained by the refinement is also 0.04. Additional broad lines in the Co 2*p* spectra are shake-up lines that come from the photoelectrons of excited ions. They show that both ions (Co^{3+} and Co^{4+}) are in a paramagnetic state [38]. The binding energies of the O 1*s* signals are listed in Table 3. Three main components come from oxygen ions and the remaining lines of larger widths are sodium Auger lines [42] and O 1*s* shake-up satellite line [43]. The component at 529.4 eV is attributed to the O 1*s* lattice

oxide, while the most intense component at 531.7 eV can be assigned to a defective oxide or hydrated oxide [44]. The third component at around 533.4 eV is assigned to the physisorbed water [45]. As we have already mentioned, the powders are hygroscopic and sensitive to moisture from air. The analyses of the Na 1*s* peaks of the pristine and the fluorinated powders indicate the existence of three and five components, respectively, but a reliable interpretation and assignments to different sodium chemical states is not straightforward. However, significant peak broadening observed for the fluorinated powder inticates a more disordered and non-uniform structure.

3.4. Magnetic properties

Generally speaking, the total susceptibility $\chi(T)$ of the investigated system can be expressed as:

$$\chi(T) = \chi_P + \chi_{dia} + \chi_{VV} + \chi_d(T) \qquad (1)$$

where χ_P, X_{dia}, X_{VV} represent Pauli paramagnetic, diamagnetic, and Van Vleck temperature independent susceptibilities, respectively. Term $\chi_d(T)$ denotes temperature-dependent Curie-Weiss paramagnetism that originates from the localized *d* electrons. Therefore, we have fitted our experimental data in the high temperature region 150–300 K to the following expression:

$$\chi(T) = \chi_0 + C/(T - \theta) \qquad (2)$$

where C represents the Curie constant, θ is the Curie-Weiss paramagnetic temperature, and χ_0 includes all temperature-independent contributions. Figure 7 shows the temperature dependence of the inverse susceptibility $1/(\chi - \chi_0)$, while the fitting parameters (C, θ, and χ_0), as well as the calculated effective magnetic moments μ_{eff} are given in Table 4. This dependence of the inverse susceptibility is linear at higher temperatures, and bellow approximately 100 K it starts to decrease more rapidly, while the magnetic phase transition temperature is observed around 25 K.

The negative Curie-Weiss paramagnetic temperatures indicate antiferromagnetically interacting spins, while the downturn of the inverse susceptibility suggests the magnetic ordering transition of a ferromagnetic type. Namely, a ferromagnetic component can be observed due to small deviations of the spins from the completely antiparallel alignment [46]. The obtained effective moments per cobalt ion are 1.13 μ_B and 1.04 μ_B, for the NCO and the NCOF samples, respectively. These values are in good agreement with previous findings for the Na_xCoO_2 ($0.7 \leq x \leq 0.8$) compounds [47–49]. Since Co^{3+} ions are in a low spin state (S=0), the obtained values of effective magnetic moments can be considered to be a contribution of Co^{4+} spins only, and the recalculated values of effective magnetic moments expressed per Co^{4+} ion are given in Table 4. It can be observed that the value for the NCO sample is above the theoretical value for low spin Co^{4+} ion (1.73 μ_B), while for the NCOF sample it is below this value. Similar behaviour has been observed in three-layered Li_xCoO_2 [50], Na_xCoO_2 [49,50], and Li/Na alternate-layered $Li_xNa_yCoO_2$ [46], and is attributed to the changed localization of the unpaired spins [50]. Namely, by decreasing the sodium content from the Na_xCoO_2 phase (by electrochemical and chemical deintercalation or, as in our case, by fluorination), the spin system is modified from the one that can be described by localized spins to the one that can be described by delocalized spins, which leads to a decreased magnetic moment per cobalt ion [49].

3.5. Electrochemical measurements

Preliminary electrochemical measurements were done to determine the differences between two powders. The results should be taken with some reservation, only as an indication of the general behaviour, since our electrochemical test cell was not fully optimized. Figure 8 presents the galvanostatic charge-discharge curves of the second cycle at C/10 current rate in the potential

range from 2 – 3.8 V. It is obvious that the fluorination of the pristine powder leads to the improvement of its electrochemical performance in terms of a higher specific capacity and lower voltage hysteresis. This is certainly the consequence of smaller crystallite size and the CoO_2 layer compression (Table 1), the latter causing weaker Na–O bonding (Table 2) and enhanced electronic conductivity. These preliminary electrochemical measurements have confirmed the predictions based on the first-principle calculations that sodium conductivity in the P2 structure increases monotonically as sodium content x decreases [33]. The described method of fluorination can be used to synthesize a series of Na_xCoO_2 powders with different sodium contents and hence different ionic conductivity. This is significant, since P2 phases with a smaller x can be obtained only through electrochemical or chemical deintercalation [51], which are more demanding and time-consuming methods.

4. Conclusion

Phase-pure Na_xCoO_2 with a P2-type structure was synthesized by a modified solid-state reaction. Fluorination was performed via a gas-solid reaction with NH_4HF_2 as a fluorinating agent. The fluorinated powder retained the P2 structure, though with a lower content of sodium. The results of the Rietveld refinement combined with the findings from the XPS measurements confirmed the $Na_{0.76}CoO_2$ and $Na_{0.44}CoO_{1.96}F_{0.04}$ compositions for the pristine and the fluorinated powders, respectively. Fluorination modifies the structure through by reducing the crystallite size and decreasing CoO_2 layer. Consequently, the fluorinated powder had an improved electrochemical performance. The described method can be used for the fluorination of other cathode materials for sodium/lithium batteries.

Acknowledgements

The Ministry of Education, Science and Technological Development of the Republic of Serbia provided financial support for this study under Grants nos. III 45004 and III 45015. The authors express their thanks to Prof. Dr. Dragan Uskoković and Dr. Max Avdeev for fruitful discussions.

References

[1] B.L. Ellis, L.F. Nazar, Sodium and sodium-ion energy storage batteries, Curr. Opin. Solid State Mater. Sci. 16 (2012) 168–177.

[2] M.H. Han, E. Gonzalo, G. Singh, T. Rojo, A comprehensive review of sodium layered oxides: powerful cathodes for Na-ion batteries, Energy Environ. Sci. 8 (2015) 81–102.

[3] L. Wang, M. Wang, D. Zhao, Thermoelectric properties of c-axis oriented Ni-substituted NaCoO 2 thermoelectric oxide by the citric acid complex method, J. Alloys Compd. 471 (2009) 519–523.

[4] M. Lee, L. Viciu, L. Li, Y. Wang, M.L. Foo, S. Watauchi, R.A. Pascal, R.J. Cava, N.P. Ong, Enhancement of the thermopower in Na_xCoO_2 in the large-x regime ($x \geq 0.75$), Phys. B. 403 (2008) 1564–1568.

[5] M.L. Foo, Y. Wang, S. Watauchi, H.W. Zandbergen, T. He, R.J. Cava, N.P. Ong, Charge Ordering, Commensurability, and Metallicity in the Phase Diagram of the Layered Na_xCoO_2, Phys. Rev. Lett. 92 (2004) 247001.

[6] K. Takada, H. Sakurai, E. Takayama-Muromachi, F. Izumi, R.A. Dilanian, T. Sasaki, Superconductivity in two-dimensional CoO_2 layers, Nature. 422 (2003) 53–55.

[7] L.W. Shacklette, T.R. Jow, L. Townsend, Rechargeable electrodes from sodium cobalt bronzes, J. Electrochem. Soc. 135 (1988) 2669–2674.

[8] C. Delmas, C. Fouassier, P. Hagenmuller, Structural classification and properties of the layered oxides, Phys. B+C. 99 (1980) 81–85.

[9] H.P. Delmas, C, Braconnier Jean-Jacques, Fouassier Claude, Electrochemical intercalation of sodium in Na_xCoO_2 bronzes, Solid State Ionics. 3/4 (1981) 165–169.

[10] R. Berthelot, D. Carlier, C. Delmas, Electrochemical investigation of the P2–Na_xCoO_2 phase diagram, Nat. Mater. 10 (2011) 74–80.

[11] M. Roger, D.J.P. Morris, D.A. Tennant, M.J. Gutmann, J.P. Goff, J.-U. Hoffmann, R. Feyerherm, E. Dudzik, D. Prabhakaran, A.T. Boothroyd, N. Shannon, B. Lake, P.P. Deen, Patterning of sodium ions and the control of electrons in sodium cobaltate, Nature. 445 (2007) 631–634.

[12] R. Ray, A. Ghoshray, K. Ghoshray, S. Nakamura, Co NMR studies of metallic $NaCo_2O_4$, Phys. Rev. B. 59 (1999) 9454.

[13] T. Motohashi, R. Ueda, E. Naujalis, T. Tojo, I. Terasaki, T. Atake, M. Karppinen, H. Yamauchi, Unconventional magnetic transition and transport behavior in $Na_{0.75}CoO_2$, Phys. Rev. B. 67 (2003) 064406.

[14] D. Baster, K. Dybko, M. Szot, K. Świerczek, J. Molenda, Sodium intercalation in Na_xCoO_{2-y} — Correlation between crystal structure, oxygen nonstoichiometry and electrochemical properties, Solid State Ionics. 262 (2014) 206–210.

[15] Q. Huang, M.L. Foo, R. A. Pascal, J.W. Lynn, B.H. Toby, T. He, H.W. Zandbergen, R.J. Cava, Coupling between electronic and structural degrees of freedom in the triangular lattice conductor Na_xCoO_2, Phys. Rev. B - Condens. Matter Mater. Phys. 70 (2004) 184110.

[16] R. Kataoka, T. Mukai, A. Yoshizawa, T. Sakai, Development of high capacity cathode material for sodium ion batteries $Na_{0.95}Li_{0.15}(Ni_{0.15}Mn_{0.55}Co_{0.1})O_2$, J. Electrochem. Soc. 160 (2013) A933–A939.

[17] J. Yoshida, E. Guerin, M. Arnault, C. Constantin, B. Mortemard de Boisse, D. Carlier, M. Guignard, C. Delmas, New P2 - $Na_{0.70}Mn_{0.60}Ni_{0.30}Co_{0.10}O_2$ layered oxide as electrode material for Na-ion batteries, J. Electrochem. Soc. 161 (2014) A1987–A1991.

[18] S. Doubaji, M. Valvo, I. Saadoune, M. Dahbi, K. Edström, Synthesis and characterization of a new layered cathode material for sodium ion batteries, J. Power Sources. 266 (2014) 275–281.

[19] Z. Tian, X. Wang, J. Liu, Z. Lin, Y. Hu, Y. Wu, Y. Wu, C. Han, Z. Hu, Power factor enhancement induced by Bi and Mn co-substitution in Na_xCoO_2 thermoelectric materials, J. Alloys Compd. 661 (2016) 161–167.

[20] D. Yuan, W. He, F. Pei, F. Wu, Y. Wu, J. Qian, Y. Cao, X. Ai, H. Yang, Synthesis and electrochemical behaviors of layered $Na_{0.67}[Mn_{0.65}Co_{0.2}Ni_{0.15}]O_2$ microflakes as a stable cathode material for sodium-ion batteries, J. Mater. Chem. A. 1 (2013) 3895–3899.

[21] D. Buchholz, A. Moretti, R. Kloepsch, S. Nowak, V. Siozios, M. Winter, S. Passerini, Toward Na-ion batteries-synthesis and characterization of a novel high capacity Na ion intercalation material, Chem. Mater. 25 (2013) 142–148.

[22] A. Windmüller, C.-L. Tsai, S. Moller, M. Balski, Y.J. Sohn, S. Uhlenbruck, O. Guillon, Enhancing the performance of high-voltage $LiCoMnO_4$ spinel electrodes by fluorination, J. Power Sources. 341 (2017) 122–129.

[23] S.-H. Kang, I. Belharouak, Y.-K. Sun, K. Amine, Effect of fluorine on the electrochemical properties of layered $Li(Ni_{0.5}Mn_{0.5})O_2$ cathode materials, J. Power Sources. 146 (2005) 650–653.

[24] P. Yue, Z. Wang, J. Wang, H. Guo, X. Xiong, X. Li, Effect of fluorine on the electrochemical performance of spherical $LiNi_{0.8}Co_{0.1}Mn_{0.1}O_2$ cathode materials via a low temperature method, Powder Technol. 237 (2013) 623–626.

[25] P. Yue, Z. Wang, H. Guo, X. Xiong, X. Li, A low temperature fluorine substitution on the electrochemical performance of layered $LiNi_{0.8}Co_{0.1}Mn_{0.1}O_{2-z}F_z$ cathode materials, Electrochim. Acta. 92 (2013) 1–8.

[26] J. Zheng, X. Wu, Y. Yang, Improved electrochemical performance of $Li[Li_{0.2}Mn_{0.54}Ni_{0.13}Co_{0.13}]O_2$ cathode material by fluorine incorporation, Electrochim. Acta. 105 (2013) 200–208.

[27] P. Yue, Z. Wang, X. Li, X. Xiong, J. Wang, X. Wu, et al., The enhanced electrochemical performance of $LiNi_{0.6}Co_{0.2}Mn_{0.2}O_2$ cathode materials by low temperature fluorine substitution, Electrochim. Acta. 95 (2013) 112–118.

[28] B.N. Wani, L.L. Miller, B.J. Suh, F. Borsa, Fluorination of Sr_2CuO_3 and high temperature superconducting oxides, Phys. C Supercond. 272 (1996) 187–196.

[29] A. Mukherjee, A. Awasthi, S. Mishra, N. Krishnamurthy, Studies on fluorination of Y_2O_3 by NH_4HF_2, Thermochim. Acta. 520 (2011) 145–152.

[30] S. Singh, J. Vanaja, V.S. Raghunathan, Process optimization for the synthesis of nanocrystalline and anhydrous lanthanide fluoride, Int. J. ChemTech Res. 7 (2015) 1537–1543.

[31] H.M. Rietveld, A profile refinement method for nuclear and magnetic structures, J. Appl. Crystallogr. 2 (1969) 65–71.

[32] R.W. Cheary, A. Coelho, A Fundamental Parameters Approach to X-ray Line-Profile Fitting, J. Appl. Crystallogr. (1992) 109–121.

[33] Y. Mo, S.P. Ong, G. Ceder, Insights into diffusion mechanisms in P2 layered oxide materials by first-principles calculations, Chem. Mater. 26 (2014) 5208–5214.

[34] C.T. Lin, D.P. Chen, J.B. Peng, P.X. Zhang, Growth and characterization of high quality single crystals of Na_xCoO_2, Phys. C. 460-462 (2007) 471–472.

[35] Y. Lei, X. Li, L. Liu, G. Ceder, Synthesis and stoichiometry of different layered sodium cobalt oxides, Chem. Mater. 26 (2014) 5288–5296.

[36] Y. Hinuma, Y. Meng, G. Ceder, Temperature-concentration phase diagram of P2-Na_xCoO_2 from first-principles calculations, Phys. Rev. B. 77 (2008) 1–16.

[37] N.S. Mcintyre, M.G. Cook, X-ray photoelectron studies on some oxides and hydroxides of cobalt, nickel, and copper, Anal. Chem. 5 (1974) 827.

[38] C.D. Wagner, W.M. Riggs, L.E. Davis, J.F.F. Moulder, G.E. Muilenberg, W.F. Stickle, P.E. Sobol, K.D. Bomben, Handbook of X-Ray Photoelectron Spectroscopy, Perkin-Elmer Corporation, 1979.

[39] J.C. Dupin, D. Gonbeau, I. Martin-Litas, P. Vinatier, A. Levasseur, Lithium intercalation / deintercalation in transition metal oxides investigated by X-ray photoelectron spectroscopy, J. Electron Spectros. Relat. Phenomena. 120 (2001) 55–65.

[40] J.C. Dupin, D. Gonbeau, H. Benqlilou-Moudden, P. Vinatier, A. Levasseur, XPS analysis of new lithium cobalt oxide thin-films before and after lithium deintercalation, Thin Solid Films. 384 (2001) 23–32.

[41] L. Chang, K. Wang, L. Huang, Z. He, H. Shao, J. Wang, Hierarchically porous CoO microsphere films with enhanced lithium/sodium storage properties, J. Alloys Compd. 725 (2017) 824–834.

[42] B. Vincent Crist, Vol 1 - XPS of Elements & Native Oxides.pdf, XPS International Inc, Iowa, USA, 1999.

[43] K.S. Kim, N. Winograd, Charge transfer shake-up sattelites in X-ray photoelectron spectra of cations and anions of $SrTiO_3$, TiO_2 and Sc_2O_3, Chem. Physucs Lett. 31 (1975) 312–317.

[44] M.C. Biesinger, B.P. Payne, A.P. Grosvenor, L.W.M. Lau, A.R. Gerson, R.S.C. Smart, Resolving surface chemical states in XPS analysis of first row transition metals, oxides and hydroxides: Cr, Mn, Fe, Co and Ni, Appl. Surf. Sci. 257 (2011) 2717–2730.

[45] X-ray photoelectron spectroscopy reference pages. http://www.xpsfitting.com/search/label/Oxygen (accessed January 1, 2018.).

[46] J.W.G. Bos, J.T. Hertz, E. Morosan, R.J. Cava, Magnetic and thermoelectric properties of layered $Li_xNa_yCoO_2$,, J. Solid State Chem. 180 (2007) 3211–3217.

[47] H. Sakurai, S. Takenouchi, N. Tsujii, E. Takayama-Muromachi, Synthesis, characterization, and magnetic properties of γ-Na_xCoO_2 ($0.70 \leq x \leq 0.84$), J. Phys. Soc. Japan. 73 (2004) 2081–2084.

[48] J.L. Gavilano, D. Rau, B. Pedrini, J. Hinderer, H.R. Ott, S.M. Kazakov, J. Karpinski, Unconventional charge ordering in $Na_{0.70}CoO_2$ below 300 K, Phys. Rev. B. 69 (2004) 100404(R).

[49] F.C. Chou, J.H. Cho, Y.S. Lee, Magnetic susceptibility study of hydrated and nonhydrated $Na_xCoO_2 \cdot yH_2O$ single crystals, Phys. Rev. B. 70 (2004) 144526.

[50] J.T. Hertz, Q. Huang, T. McQueen, T. Klimczuk, J.W.G. Bos, L. Viciu, R.J. Cava, Magnetism and structure of Li_xCoO_2 and comparison to Na_xCoO_2, Phys. Rev. B. 77 (2008) 075119.

[51] J. Molenda, D. Baster, A. Milewska, K. Świerczek, D.K. Bora, A. Braun, J. Tobola, Electronic origin of difference in discharge curve between Li_xCoO_2 and Na_xCoO_2 cathodes, Solid State Ionics. 271 (2015) 15–27.

Table 1. The results of the Rietveld refinements of the NCO and the NCOF powders. The standard deviations are given in parentheses.

Sample	NCO	NCOF
Lattice parameters [Å]	$a = b =$ 2.8374(3), c = 10.868(2)	$a = b$ = 2.8272(3), c = 10.937 (2)
Primitive cell volume [$Å^3$]	75.77(1)	75.71(2)
Mean crystallite size [nm]	117(6)	73(3)
Microstrain [%]	0	0.12(7)
Strain [%%]	0.25(4)	0
Free coordinate O^{2-}, z	z = 0.0840(8)	z = 0.0644(9)
Na(1) site occ.	0.25(1)	0.17(1)
Na(2) site occ.	0.51(1)	0.27(1)
O site occ. by F	-	0.02(1)
Preferred orientation normal to c axis	1.005(7)	0.943(8)
NaO_2 interslab thickness [Å]	3.6096(5)	4.0817(6)
CoO_2 slab thickness [Å]	1.823(1)	1.3868(4)
Interslab distance [Å]	5.433(1)	5.469(2)
Weight percent of NaF [%]	0	2.8(4)
R_{wp} factor [%]	1.09	1.06

Table 2. Selected bond distances and bond angles in the NCO and the NCOF powders.

Sample	NCO	NCOF
Bonded atoms	Bond length [Å]	Bond length [Å]
Co-O	1.875(4)	1.778(4)
Co-Co	2.8374(5)	2.8272(5)
Na(1) - O	2.437(6)	2.605(8)
Na(2) - O	2.437(6)	2.605(8)
Bonded atoms	Bond angles [º]	Bond angles [º]
Co – O – Co	98.3(2)	105.3 (2)
O – Co – O	81.7(2)	74.7(2)
O – Co – O	98.3(2)	105.3(2)
O – Co – O	180.0(3)	180.0(4)

Table 3. Electron binding energies for the NCO and the NCOF samples.

Sample	Binding energy (eV)	FWHM (eV)	Peak assignment
Co 2*p*			
NCO	779.8 – 794.9	1.5 – 1.6	Co $2p_{3/2-1/2}$ (III)
	781.1 – 796.4	1.5 – 1.6	Co $2p_{3/2-1/2}$ (IV)
	782.6	3.2	satellite Co(IV)
	789.7	4.7	satellite Co(III)
	797.6	3.0	satellite Co(IV)
NCOF	779.9-794.9	1.6 – 1.7	Co $2p_{3/2-1/2}$ (III)
	781.2-796.3	1.6 – 1.7	Co $2p_{3/2-1/2}$ (IV)
	783.7	4.2	satellite Co(IV)
	789.1	5.8	satellite Co(III)
	797.7	3.3	satellite Co(IV)
	804.4	3.6	satellite Co(III)
O 1*s*			
NCO	523.8	2.7	Na Auger line
	529.4	1.2	Lattice oxygen
	531.7	1.8	Defective oxide or hydroxide
	533.4	1.8	Physisorbed water
	536.0	2.7	Na Auger line
NCOF	524.8	3.5	Na Auger line
	529.2	1.5	Lattice oxygen
	531.8	2.1	Defective oxide or hydroxide
	533.2	2.1	Physisorbed water
	536.2	5.5	Na Auger line
	540.2	3.1	O 1s satellite

Table 4.The fitting parameters C, θ, χ_0, and the calculated effective magnetic moments μ_{eff} for the NCO and the NCOF powders.

Sample	C [emu·K/mol·Oe]	Θ [K]	χ_0 [emu·K/mol·Oe]	μ_{eff} per Co [μ_B]	μ_{eff} per Co^{4+} [μ_B]
NCO	0.1595	- 90	0.0000664	1.13	2.31
NCOF	0.1359	- 77	0.000182	1.04	1.45

Figure captions

Figure 1. The structure of the P2 type Na_xCoO_2.

Figure 2. FESEM images of the NCO powder with denoted particle sizes (a) and a particle with a laminar structure (b).

Figure 3. FESEM images of the NCOF powder with denoted particle sizes (a) and a particle with a laminar structure (b).

Figure 4. The observed (•), calculated (—), and the difference between the observed and calculated (bottom) X-ray diffraction data taken at room temperature for the NCO and the NCOF powders. The vertical markers below the diffraction patterns indicate the positions of possible Bragg reflections for the P2 -Na_xCoO_2 and NaF phases (for the NCOF sample).

Figure 5. The survey photoelectron spectra of the NCO (a) and the NCOF (b) powders.

Figure 6. X-ray photoelectron high-resolution scans of Co 2p (a), O 1s (b), and Na 1s (c).

Figure 7. The temperature dependences of the inverse magnetic susceptibilities for the NCO (a) and the NCOF (b) powders. Solid lines are fits to the Curie Weiss law.

Figure 8. The charge and discharge curves of the NCO (a) and the NCOF (b) powders at C/10 current rate.

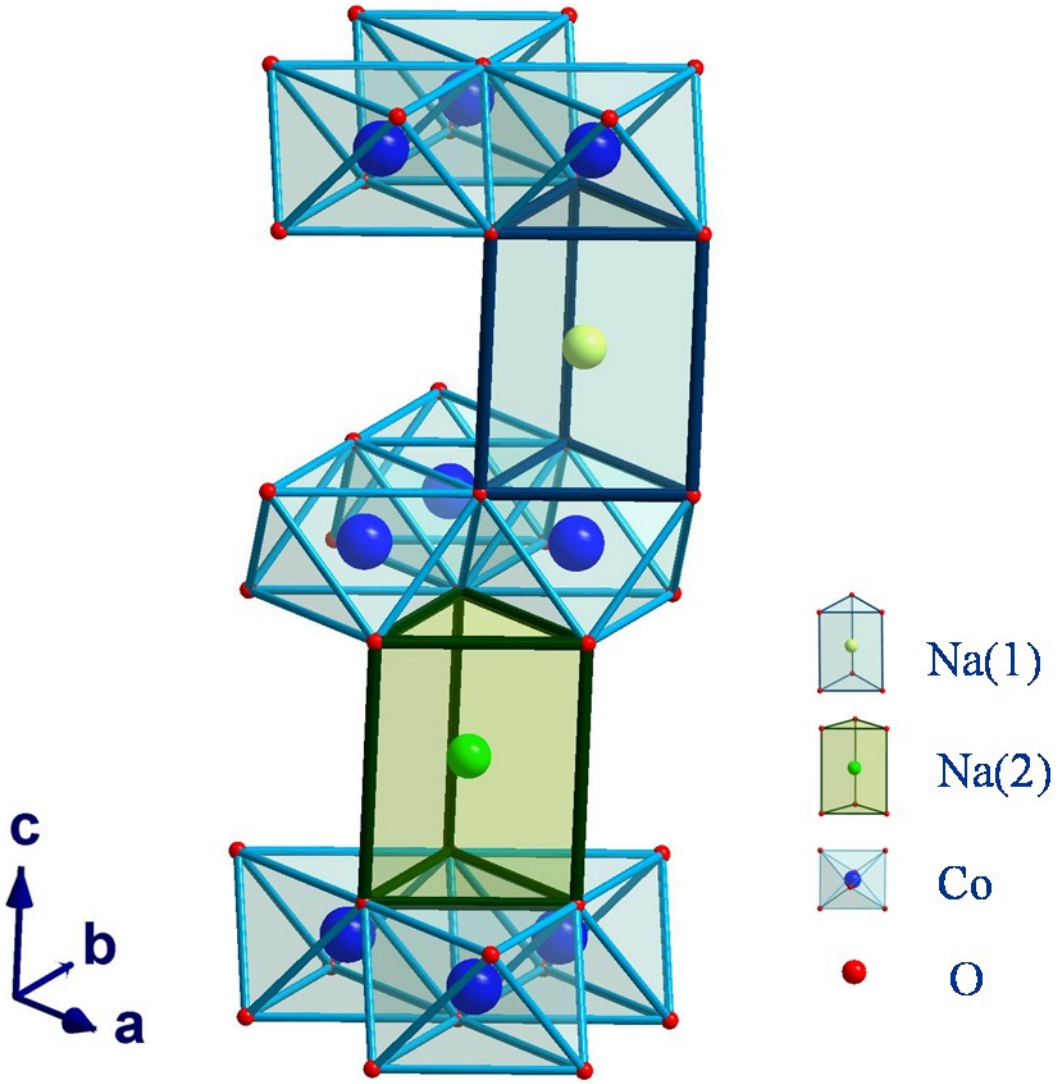

Figure 1.

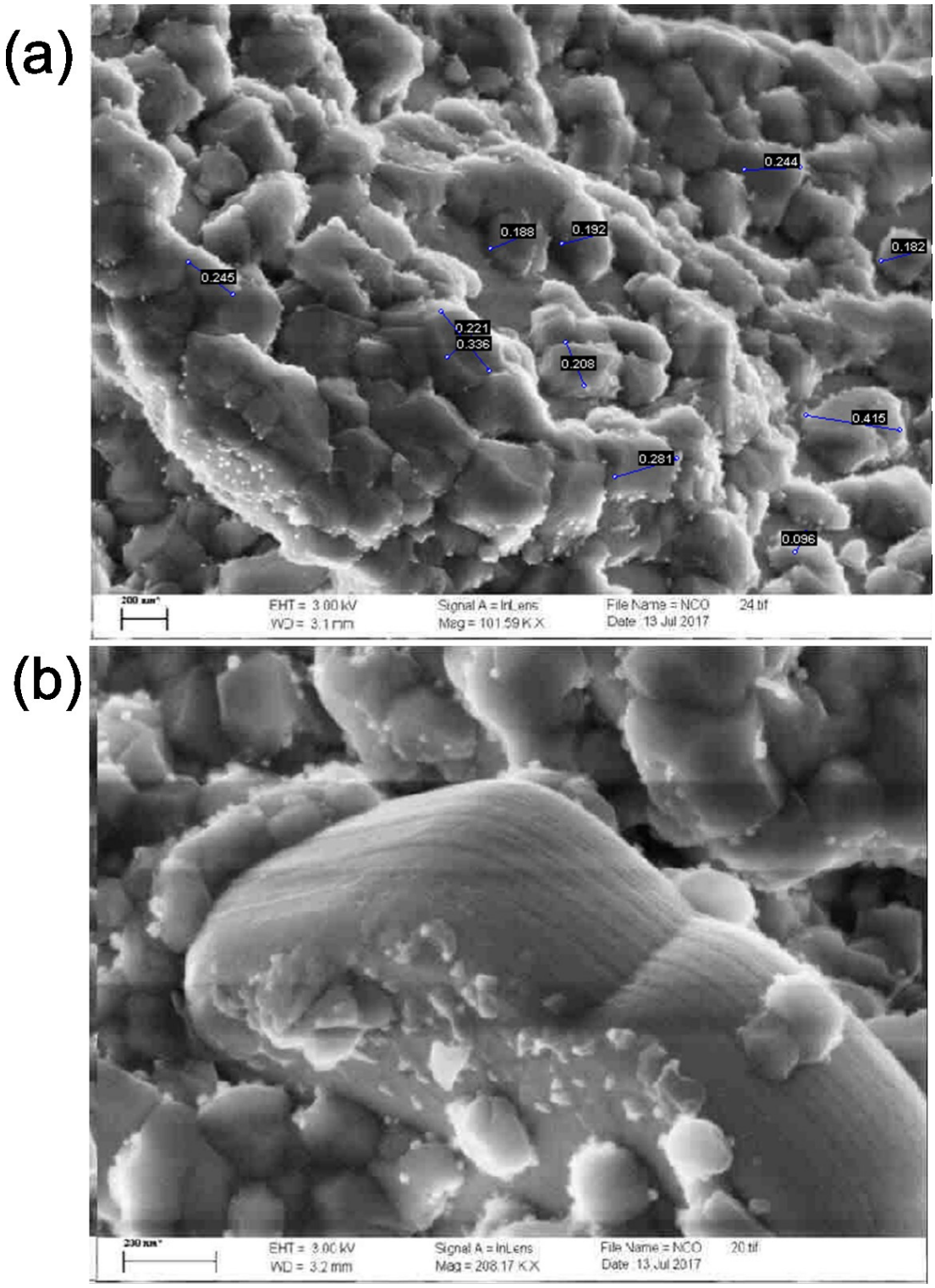
(a)
0.244
0.188
0.192
0.182
0.245
0.221
0.336
0.208
0.415
0.281
0.096
200 nm
EHT = 3.00 kV
WD = 3.1 mm
Signal A = InLens
Mag = 101.59 K X
File Name = NCO 24.tif
Date :13 Jul 2017
(b)
200 nm
EHT = 3.00 kV
WD = 3.2 mm
Signal A = InLens
Mag = 208.17 K X
File Name = NCO 20.tif
Date :13 Jul 2017

Figure 2.

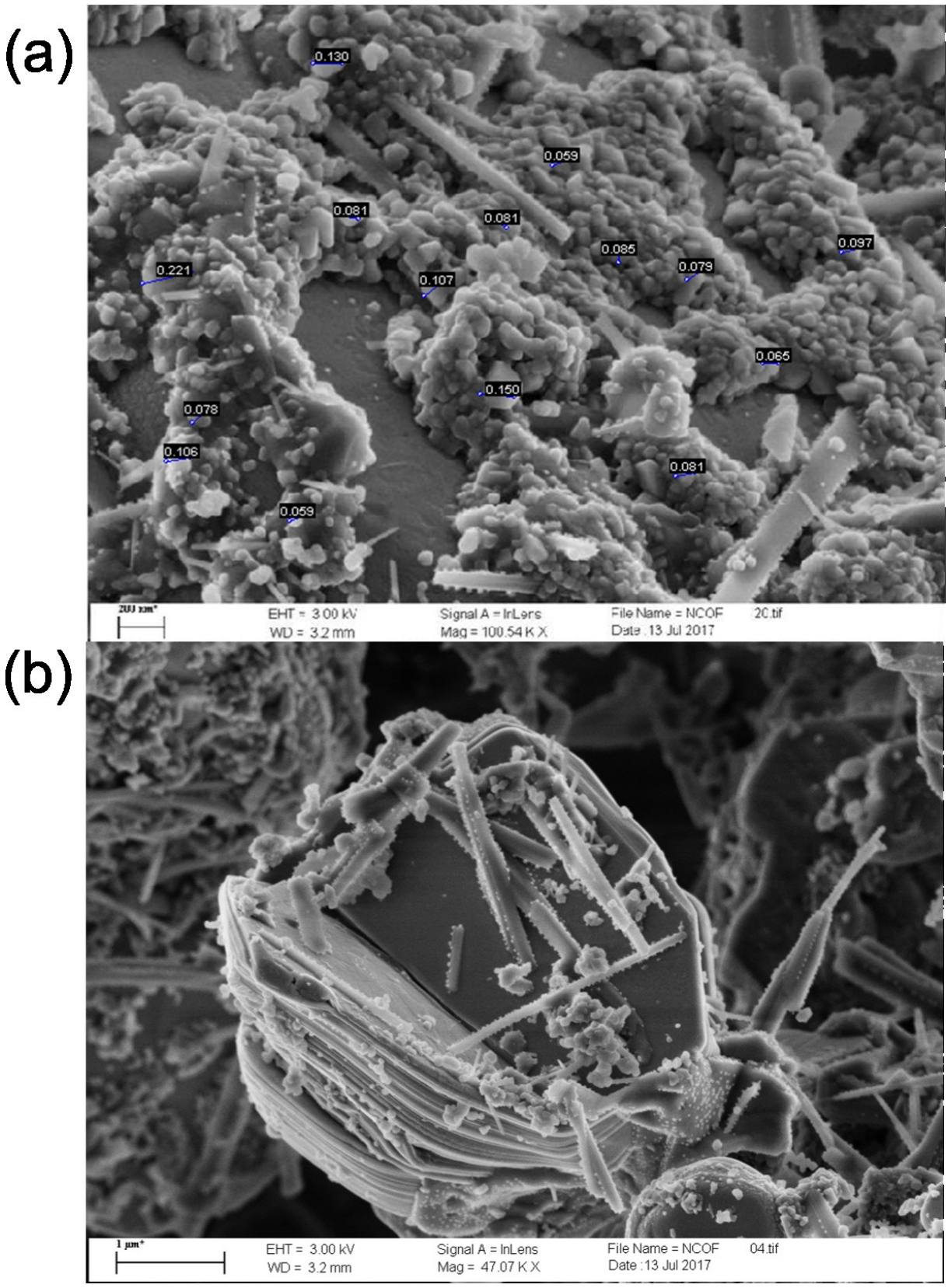
(a)
0.130
0.059
0.081
0.081
0.085
0.097
0.221
0.107
0.079
0.065
0.150
0.078
0.106
0.081
0.059
EHT = 3.00 kV
WD = 3.2 mm
Signal A = InLens
Mag = 100.54 K X
File Name = NCOF 20.tif
Date :13 Jul 2017
(b)
1 µm
EHT = 3.00 kV
WD = 3.2 mm
Signal A = InLens
Mag = 47.07 K X
File Name = NCOF 04.tif
Date :13 Jul 2017

Figure 3.

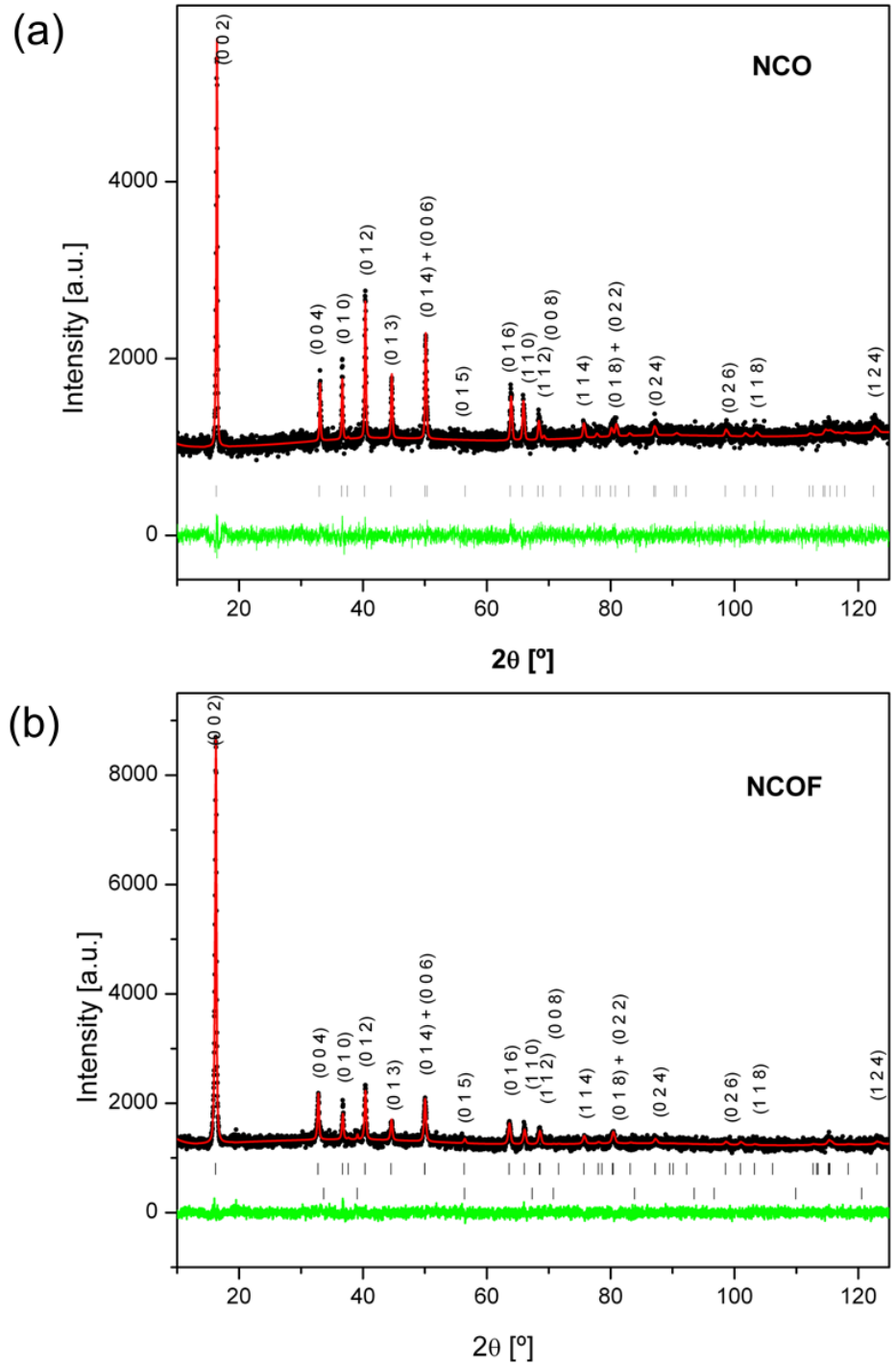
(a)
NCO
Intensity [a.u.]
2θ [º]
(0 0 2)
(0 0 4)
(0 1 0)
(0 1 2)
(0 1 3)
(0 1 4) + (0 0 6)
(0 1 5)
(0 1 6)
(1 1 0)
(1 1 2)
(0 0 8)
(1 1 4)
(0 1 8) + (0 2 2)
(0 2 4)
(0 2 6)
(1 1 8)
(1 2 4)
(b)
NCOF
Intensity [a.u.]
2θ [º]

Figure 4.

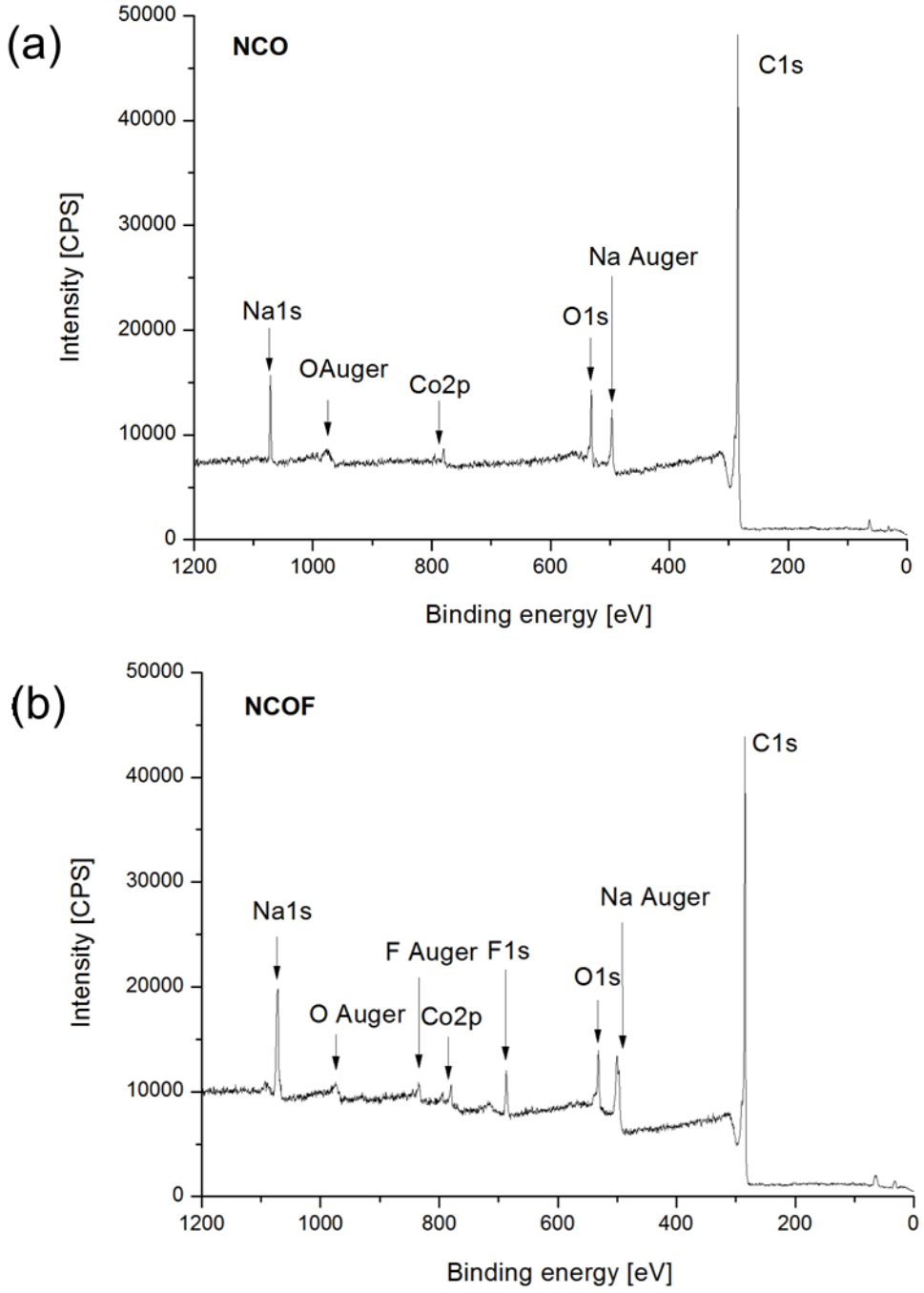
(a)
NCO
C1s
Na Auger
Na1s
O1s
OAuger
Co2p
Intensity [CPS]
Binding energy [eV]
(b)
NCOF
C1s
Na Auger
Na1s
F Auger F1s
O1s
O Auger
Co2p
Intensity [CPS]
Binding energy [eV]

Figure 5.

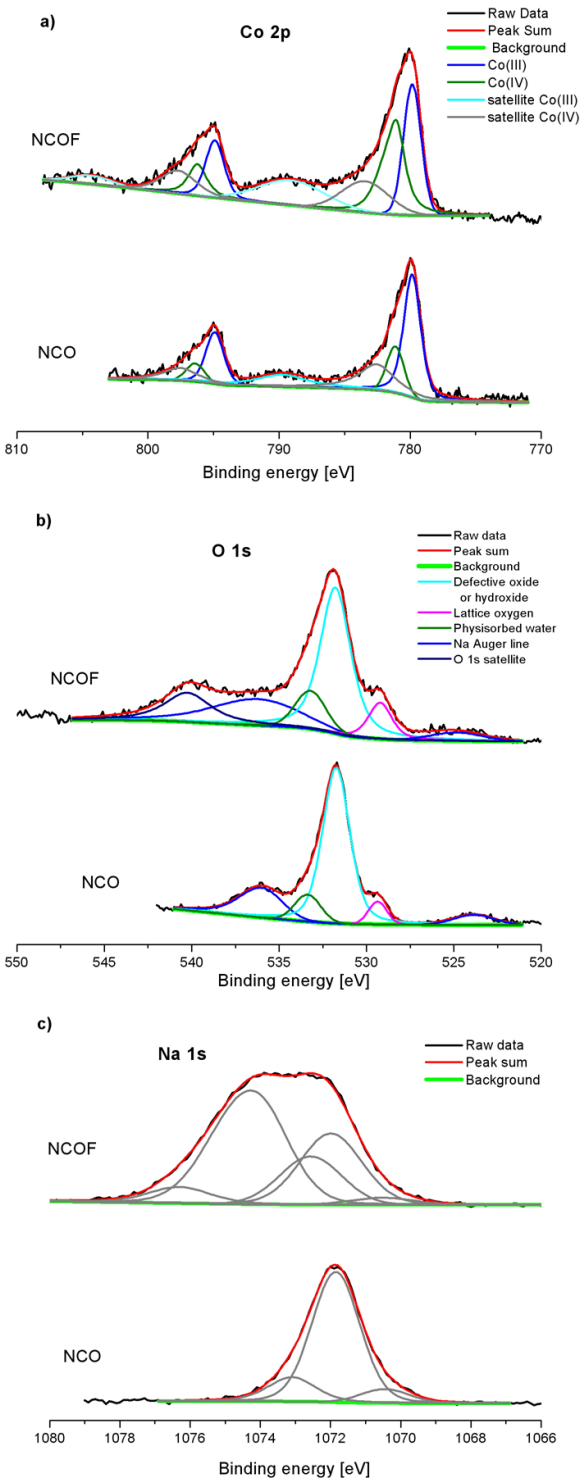
a)
Co 2p
Raw Data
Peak Sum
Background
Co(III)
Co(IV)
satellite Co(III)
satellite Co(IV)
NCOF
NCO
810
800
790
780
770
Binding energy [eV]
b)
O 1s
Raw data
Peak sum
Background
Defective oxide
or hydroxide
Lattice oxygen
Physisorbed water
Na Auger line
O 1s satellite
NCOF
NCO
550
545
540
535
530
525
520
Binding energy [eV]
c)
Na 1s
Raw data
Peak sum
Background
NCOF
NCO
1080
1078
1076
1074
1072
1070
1068
1066
Binding energy [eV]

Figure 6.

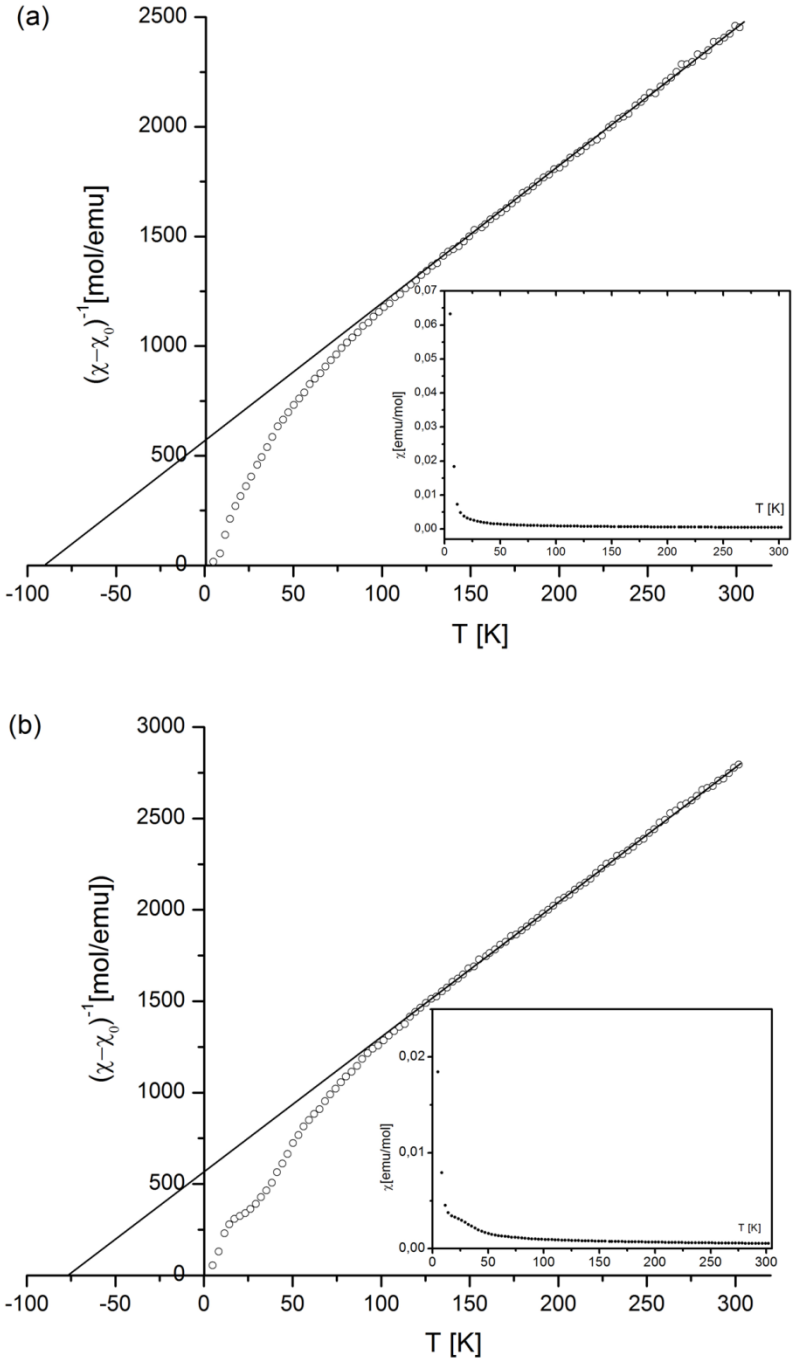
(a)
2500
2000
1500
1000
500
0
-100
-50
0
50
100
150
200
250
300
T [K]
$(\chi-\chi_0)^{-1}$[mol/emu]
0,07
0,06
0,05
0,04
0,03
0,02
0,01
0,00
χ[emu/mol]
T [K]
(b)
3000
2500
2000
1500
1000
500
0
-100
-50
0
50
100
150
200
250
300
T [K]
$(\chi-\chi_0)^{-1}$[mol/emu])
0,02
0,01
0,00
χ[emu/mol]
T [K]

Figure 7.

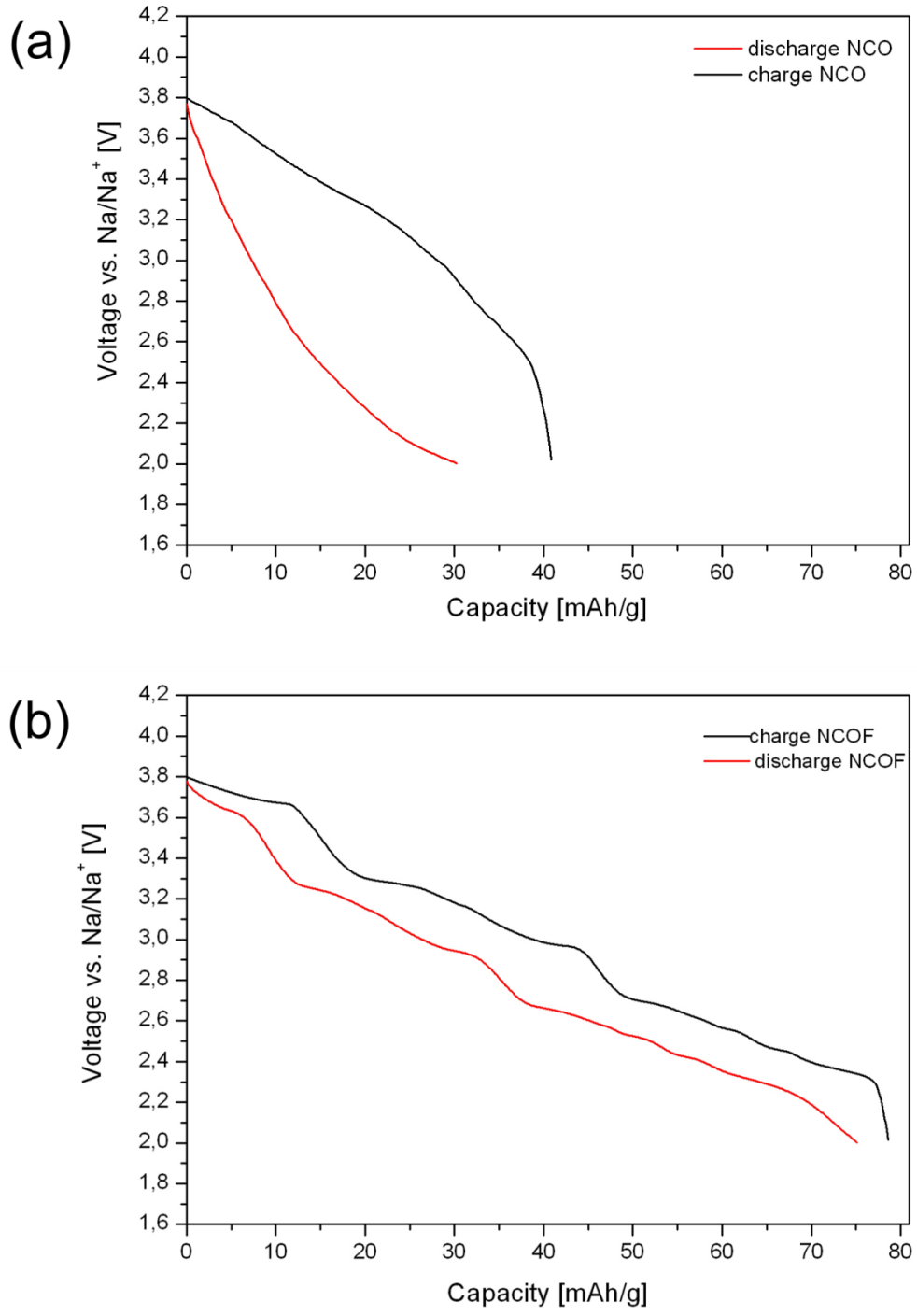
(a)
discharge NCO
charge NCO
Voltage vs. Na/Na+ [V]
Capacity [mAh/g]
(b)
charge NCOF
discharge NCOF
Voltage vs. Na/Na+ [V]
Capacity [mAh/g]

Figure 8.